Systemic consequences of disorder in magnetically self-organized topological $MnBi_2Te_4/(Bi_2Te_3)_n$ superlattices

To cite this article: Joanna Sitnicka *et al* 2022 *2D Mater.* **9** 015026

2D Materials

OPEN ACCESS

RECEIVED
21 September 2021

REVISED
15 November 2021

ACCEPTED FOR PUBLICATION
24 November 2021

PUBLISHED
13 December 2021

PAPER

Systemic consequences of disorder in magnetically self-organized topological $MnBi_2Te_4/(Bi_2Te_3)_n$ superlattices

Joanna Sitnicka[1], Kyungwha Park[2], Paweł Skupiński[3], Krzysztof Grasza[3], Anna Reszka[3], Kamil Sobczak[4], Jolanta Borysiuk[1], Zbigniew Adamus[3], Mateusz Tokarczyk[1], Andrei Avdonin[3], Irina Fedorchenko[5], Irina Abaloszewa[3], Sylwia Turczyniak-Surdacka[4], Natalia Olszowska[6], Jacek Kołodziej[6,7], Bogdan J Kowalski[3], Haiming Deng[8], Marcin Konczykowski[9], Lia Krusin-Elbaum[8] and Agnieszka Wołoś[1,*]

[1] Faculty of Physics, University of Warsaw, ul. Pasteura 5, 02-093 Warsaw, Poland
[2] Department of Physics, Virginia Tech, 850 West Campus Drive, Blacksburg, VA 24061, United States of America
[3] Institute of Physics, Polish Academy of Sciences, Aleja Lotników 32/46, PL-02668 Warsaw, Poland
[4] Faculty of Chemistry, Biological and Chemical Research Centre, University of Warsaw, ul. Zwirki i Wigury 101, 02-089 Warsaw, Poland
[5] Kurnakov Institute of General and Inorganic Chemistry, Russian Academy of Sciences, Leninskii prosp. 31, Moscow 117901, Russia
[6] National Synchrotron Radiation Centre SOLARIS, Jagiellonian University, ul. Czerwone Maki 98, 30-392 Cracow, Poland
[7] Faculty of Physics, Astronomy and Applied Computer Science, Jagiellonian University, ul. prof. Stanisława Łojasiewicza 11, 30-348 Cracow, Poland
[8] Department of Physics, The City College of New York–CUNY, 85 St. Nicholas Terrace, New York, NY 10027, United States of America
[9] Laboratoire des Solides Irradiés, CEA/DRF/IRAMIS, Ecole Polytechnique, CNRS, Institut Polytechnique de Paris, F-91128 Palaiseau, France
[*] Author to whom any correspondence should be addressed.

E-mail: agnieszka.wolos@fuw.edu.pl

Keywords: topological insulators, disorder, magnetism, quantum anomalous Hall effect, FMR, ARPES, DFT

Supplementary material for this article is available online

Abstract

$MnBi_2Te_4/(Bi_2Te_3)_n$ materials system has recently generated strong interest as a natural platform for the realization of the quantum anomalous Hall (QAH) state. The system is magnetically much better ordered than substitutionally doped materials, however, the detrimental effects of certain disorders are becoming increasingly acknowledged. Here, from compiling structural, compositional, and magnetic metrics of disorder in ferromagnetic (FM) $MnBi_2Te_4/(Bi_2Te_3)_n$ it is found that migration of Mn between $MnBi_2Te_4$ septuple layers (SLs) and otherwise non-magnetic Bi_2Te_3 quintuple layers (QLs) has systemic consequences—it induces FM coupling of Mn-depleted SLs with Mn-doped QLs, seen in ferromagnetic resonance as an acoustic and optical resonance mode of the two coupled spin subsystems. Even for a large SL separation ($n \gtrsim 4$ QLs) the structure cannot be considered as a stack of uncoupled two-dimensional layers. Angle-resolved photoemission spectroscopy and density functional theory studies show that Mn disorder within an SL causes delocalization of electron wave functions and a change of the surface band structure as compared to the ideal $MnBi_2Te_4/(Bi_2Te_3)_n$. These findings highlight the critical importance of inter- and intra-SL disorder towards achieving new QAH platforms as well as exploring novel axion physics in intrinsic topological magnets.

1. Introduction

Searching for materials suitable for the realization of the quantum anomalous Hall (QAH) effect or axion insulator state [1–6] led recently to an explosive interest in $MnBi_2Te_4$ family, and in particular in a self-organized $MnBi_2Te_4/(Bi_2Te_3)_n$. Both the bulk compounds and the $MnBi_2Te_4/(Bi_2Te_3)_n$ thin films have rich topological phase diagrams in which the stacking sequence of magnetic septuple layers (SLs) and non-magnetic quintuple layers (QLs) plays a key role [7, 8]. In these systems the magnetic $MnBi_2Te_4$ SLs are structurally and compositionally compatible with the non-magnetic Bi_2Te_3 topological

insulator [9–15]. When $MnBi_2Te_4$ is located on the top surface of the structure the topological surface states (TSSs) are expected to appear in the magnetic material, which in contrast to weak proximity effects studied earlier [16] causes giant opening of the Dirac gap and a strong modification of spin texture of the TSSs [9, 13, 17–19]. Manganese self-organizes planarly while also doping Bi_2Te_3, where at low doping level it preferentially substitutes on the Bi sites, akin to doping in Bi_2Se_3 [20]. Increased doping results in Mn entering an interstitial position in the van der Waals gap [21]. When doping exceeds about 2 at.%, Mn self-organizes into $MnBi_2Te_4$ SLs within the Bi_2Te_3 matrix [3, 13]. Although this system is magnetically much better organized than the substitutionally doped materials [22], it is not free from the disorder, which can arise from (a) statistical distribution of SLs, (b) magnetic disorder within SLs, or (c) doping of Mn into Bi_2Te_3 QLs. These three highlighted effects strongly impact both magnetism and the surface band structure. Thus, in order to get a controllable access to the magneto-topological phenomena the disorder should be understood and mastered.

The disorder effects have been very recently recognized in the family of $MnBi_2Te_4/(Bi_2Te_3)_n$ or in compounds containing Sb as a driving force for ferromagnetism (FM) in otherwise antiferromagnetic (AFM) material [19, 23]. This led to some basic questions regarding the role of the disorder in a broader sense. In particular, the fundamental question concerns the effects of disorder on surface electronic band structure and on magnetic order. Presently, there is insufficient knowledge of the magnetic ordering of manganese ions in a composite $MnBi_2Te_4/(Bi_2Te_3)_n$, complicated by the Mn site mixing, since both intra-layer and inter-layer coupling comes into play, dependent on the Mn–Mn distance in SLs and on the non-uniformly distributed other possible Mn defect sites. The effect of disorder on the surface electronic band structure also requires deeper understanding, due to the abundance of experimentally observed electronic bands and the still somewhat unclear situation with the temperature dependence of the Dirac mass gap [11, 13, 19]. Recent reports suggest a possibly harmful influence of the disorder on the band inversion necessary to obtain topological insulator phase [15, 23]. On the other hand, classifying and controlling the effects of disorder can lead to a better understanding of the QAH state [24].

In this work, we show results of structural and chemical composition investigations of FM $MnBi_2Te_4/(Bi_2Te_3)_n$, with n between 2 and 12 and the Curie temperature, T_c, ranging between 6 K and 13 K, and correlate it with magnetic properties studied by ferromagnetic resonance (FMR) and with properties of electronic surface band structure investigated by angle-resolved photoemission spectroscopy (ARPES) and density functional theory (DFT). Our structural and chemical composition studies show the omnipresent migration of Mn between $MnBi_2Te_4$ SLs and Bi_2Te_3 QLs. In order to investigate FM in these disordered structures, we applied X-band FMR, a technique that is complementary to standard magnetometric measurements and brings additional information about the magnetic system. In particular, the FMR has been widely applied to ultrathin films allowing investigation of the interlayer exchange coupling [25–28]. The Mn site mixing between SLs and QLs changes this material systemically making it akin to a stack of exchange-coupled ultra-thin magnetic films of $Mn_xBi_{3-x}Te_4$ and $(Bi,Mn)_2Te_3$. The surface electronic states become delocalized under disorder and the structure of the bands changes compared to the ideal $MnBi_2Te_4/(Bi_2Te_3)_n$ as seen both in ARPES and DFT.

2. Disorder modifications of structural properties and chemical composition

All $MnBi_2Te_4/(Bi_2Te_3)_n$ samples studied in this work show almost uniform distribution of the elements in the energy dispersive x-ray (EDX) analysis on submicron scale accessible in SEM, with the average Mn concentration 2 or 4 at.%, respectively (table 1). Neither inhomogeneities of the chemical composition nor Mn inclusions are observed. In contrast, transmission electron microscopy (TEM) studies of the same samples performed on nm or sub-nanometer scale reveal presence of self-organized SLs of $MnBi_2Te_4$ incorporated into Bi_2Te_3 matrix (figures 1(a) and (b)). Manganese is planarly distributed in the middle of a SL while the SL and the neighboring QL are separated by a van der Waals gap. Although all samples (except for S4) have the same average Mn concentration, Mn can be distributed in different ways. The largest separation between SLs, $n = 12$ QLs in the $MnBi_2Te_4/(Bi_2Te_3)_n$ formula, is found in S1 sample obtained by the vertical variant of the Bridgman method after the synthesis only. Small statistical distribution with standard deviation (SD) of five QLs can be observed (figure 1(c)). The superlattice $MnBi_2Te_4/(Bi_2Te_3)_n$ disordered with respect to n covers the entire investigated area without detected larger blocks of Bi_2Te_3. After crystallization, sample S2, SLs are rearranged keeping a preferential distance of four QLs and a grouping in a superlattice containing multiples of mostly three SLs (can be three, six, or more rarely nine SLs). Small variation of the distance between SLs occurs and the multiplets are separated from each other by larger Bi_2Te_3 blocks as seen in figure 1(f). The SLs extend, without breaking their continuity, all across the investigated 1 μm wide lamella and cover the entire length of the lamella, extending to a distance of 16 μm. Sample S3 obtained by the horizontal variant of the Bridgman method has a medium separation between SLs with mean value of about seven QLs (SD = 1 QL). A break in the continuity of SLs is often observed in this sample

Table 1. Structural and magnetic parameters of $MnBi_2Te_4/(Bi_2Te_3)_n$ mean distance between SLs (n), average Mn concentration in a sample from SEM-EDX and Mn concentration in SLs from TEM-EDX, respectively, the critical temperature for bulk FM phase transition (T_c) from magnetometric or magnetotransport measurements. Mn concentration in QLs is typically between 0.3 and 1 at.% indicated by TEM-EDX, except for S4—about 2.9 at.%. Note that for sample S2, $MnBi_2Te_4/(Bi_2Te_3)_n$ superlattice is actually embedded in the Bi_2Te_3 matrix.

No.	n (QLs)	Mn average (at.%)	Mn in SLs (at.%)	T_c (K)
S1	12 ± 5	2	4.4 ± 0.7	6
S2	4	2	10.6 ± 1.6	13
S3	7 ± 1	2	5.0 ± 0.8	10
S4	2	4	7.6 ± 1.1	10

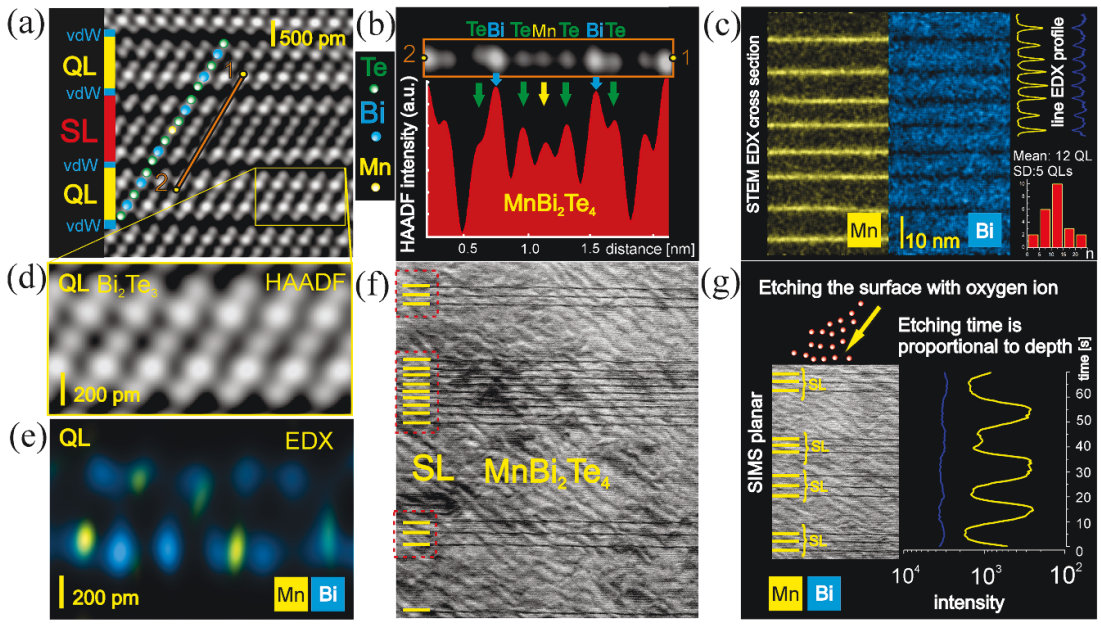

Figure 1. Structure and composition of $MnBi_2Te_4/(Bi_2Te_3)_n$. (a) HAADF-STEM image with intensity profile (b) of a SL in QL matrix. Bi as the heaviest element gives the highest intensity to the image. Manganese is incorporated in the middle layer of the SL. SL and neighboring QL are separated by the van der Waals gap. (c) Fragment of $MnBi_2Te_4/(Bi_2Te_3)_n$ superlattice in sample S1. EDX mapping with the distribution of Mn atoms shown in yellow and Bi atoms shown in blue, respectively. A histogram showing the statistical distribution of the distance between SLs with a mean distance of 12 QLs and standard deviation of 5 QLs is presented. (d) HAADF-STEM image and corresponding EDX mapping (e) showing Mn atoms substituting Bi site in a QL of sample S1. (f) STEM image showing the grouping of SLs in superlattices containing multiple of three SLs in sample S2. The distance between SLs remains roughly constant, four QLs. (g) SIMS depth profile of sample S2 showing structures due to the superlattice formed by the SLs in the QL matrix. In QLs the concentration of Mn is about ten times lower than in SLs, consistently with EDX evaluations.

where SLs interchange with QLs. Finally, sample S4 (horizontal Bridgman) has a very uniform morphology and the smallest distance between SLs of two QLs. This sample has higher average Mn concentration, about 4 at.%. Different characteristics of the four samples are summarized in table 1.

Nano-structural studies show omnipresent migration of Mn between SLs and QLs. EDX analysis performed on nm scale of TEM reveals a dearth of Mn in SLs and a simultaneous presence of Mn in QLs. The highest Mn concentration in SLs, 10.6 ± 1.6 at.%, is found in sample S2. This agrees within three sigma limit to the nominal value of the $MnBi_2Te_4$ formula ($\sim$14 at.%) and simultaneously S2 sample has the highest FM phase transition temperature 13 K. The companion sample that did not undergo the second step in the Bridgman growth process, sample S1, shows much lower Mn concentration in SLs, 4.4 ± 0.7 at.%, affirming that the crystallization in temperature gradient leads to significant improvement of the $MnBi_2Te_4$ structure. Finally, samples S3 and S4 show 5.0 ± 0.8 at.% and 7.6 ± 1.1 at.% of Mn in SLs, respectively (table 1).

Remarkably, Mn is not only present in the $MnBi_2Te_4$ SLs but also substitutes on Bi sites in the Bi_2Te_3 QLs. The sparse Mn population in QLs is clearly indicated by the TEM-EDX analysis between 0.3 and 1 at.% in all samples. Figures 1(d) and (e) show high-angle annular dark field scanning transmission electron microscopy (HAADF-STEM) image compared to the corresponding EDX map in high resolution showing Mn substituting Bi in a Bi_2Te_3 QL. Secondary ion mass spectroscopy (SIMS) data are further consistent with the EDX analysis. The SIMS depth profile of Mn and Bi (figure 1(g)) reveals a fragment of the superlattice structure originating from

groups of three SLs split by four QLs, which are further separated by larger QL blocks. The increase of the Mn signal intensity and the accompanying decline of the Bi intensity are clearly revealed. In some cases, peaks marking the position of a single SL are resolved as well, indicating a highly ordered layered structure extending on an area covered by the beam spot of one squared mm in diameter. The intensity of the Mn SIMS signal between peaks (in QL regions) is about ten times lower than at the peaks, consistently with EDX evaluations of Mn concentration in SLs and in QLs, respectively. Mn preferentially substitutes on Bi sites in QLs which, however, does not change the general arrangement of the crystallographic structure. The ubiquitous Mn/Bi intermixing in the $MnBi_2Te_4$ family has been earlier suggested in the literature reports as well [11, 23, 29]. It will be discussed below that the disorder in the distribution of Mn, in particular, doping of Mn into QLs and depletion of SLs affects strongly both the magnetic properties and the surface electron band structure.

3. Disorder-induced magnetic behaviors detected in FMR

It has been established that the intra-layer ordering within a model $MnBi_2Te_4$ single layer is FM with the phase transition temperature of about 12 K, regardless of the thickness of the $MnBi_2Te_4$ film or interfacing with other layered material through the van der Waals gap [12]. In the three-dimensional $MnBi_2Te_4$ ($n = 0$) built of SLs separated by van der Waals gaps, the inter-layer coupling is AFM with bulk critical temperature increased up to 24–25 K by Anderson superexchange, which stabilizes the system and enhances the critical temperature above that for a single layer [10, 12]. Weakness of the inter-layer coupling and its oscillating character in $MnBi_2Te_4/(Bi_2Te_3)_n$ ($n > 0$) does not allow to predict theoretically the FM or AFM order type and a critical temperature of the bulk magnetic phase for n higher than 0, thus all the conclusions must rely on the experiment. In the experiment, $MnBi_2Te_4/(Bi_2Te_3)_n$ with $n = 1$–3 show effects of inter-layer decoupling manifested by a strong drop of Néel temperature, T_N, with increased distance between SLs, from 25 K for $n = 0$ down to 13 K for $n = 1$ and 11.9 K for $n = 2$ [10]. Remarkably, for $n = 2$ the FM bulk ordering has been reported next to the AFM [19, 29], which is consistent with similarly calculated energy of FM and AFM ground states [10, 30], making the system particularly vulnerable to disorder effects. For $n = 3$ and higher the vanishing exchange coupling between SLs has been reported [10, 30]. Moreover, it has been shown that the inter-layer exchange coupling, so important in determining the magnetic properties in the $MnBi_2Te_4/(Bi_2Te_3)_n$ family, can be tuned by lattice engineering using pressure as well as chemical substitution [31]. The possibility of weak coupling of SLs via long-range RKKY interaction mediated by free carriers has not been excluded [10], however, our earlier studies show that there is no evidence for that [3]. On the other hand, the role of Mn in QLs in the stabilization of the bulk ferrimagnetic phase has recently been postulated [19]. This issue will be explored below.

In contrast to the AFM materials studied extensively before, samples investigated in this work, with n between 2 and 12, show FM response in magnetometry and/or magnetotransport with Curie temperatures between 6 K and 13 K, respectively (table 1). The T_c below the critical temperature of a single $MnBi_2Te_4$ layer can be accounted for missing Mn in a SL, as it is seen in structural studies (section 2), since the intra-layer exchange coupling will be reduced with highly increased distance between Mn sites. On the other hand, the presence of Mn in QLs cannot be ignored and the resulting critical temperature is thus a combined effect of the magnetic disorder in a single SL and the coupling of SLs via Mn in QLs. It has been established earlier that the pure QL-material $Bi_{2-x}Mn_xTe_3$ with Mn concentration around 0.8–1.8 at.% creates an FM phase as well, with $T_c = 9$–12 K, respectively [32, 33].

It has been established, that magnetic resonance in two coupled ultra-thin films consists of two eigenmodes formed by the uniform modes of the individual layers, the acoustic mode for which the magnetization precession of both films occurs in-phase and the weaker optical mode where the mutual precession is out-of-phase [25–28]. In the case of ferromagnetically coupled films, the acoustic mode appears at the higher magnetic field than the optical mode while for AFM coupling the situation is the opposite and the acoustic mode is located at the lower magnetic field than the optical mode. This feature allows distinguishing the type of coupling between magnetic layers.

The acoustic and optical modes of the coupled SL and Mn doped QL spin subsystems are clearly resolved at low temperatures for sample S2 ($n = 4$), which has the highest crystal uniformity followed by the lowest FMR line width and the highest T_c (figure 2(a)). The stronger acoustic mode is located at a higher magnetic field than the weaker optical mode allowing to assign the resonance to the FM coupling. This finding contrasts with the recently proposed conceptual Ising model suggesting AFM coupling between SLs and Mn in QLs [19]. Here, the discrepancy may arise from the simplicity of the theoretical approach applied to the complex disordered spin system, in particular disregarding intra-layer disorder in an SL. A small difference in the amplitude ($I_{ac}/I_{opt} = 1.8$) and in the position of the two modes (figure 2(d)) indicates a rather small value of the inter-layer coupling parameter, which will be discussed below.

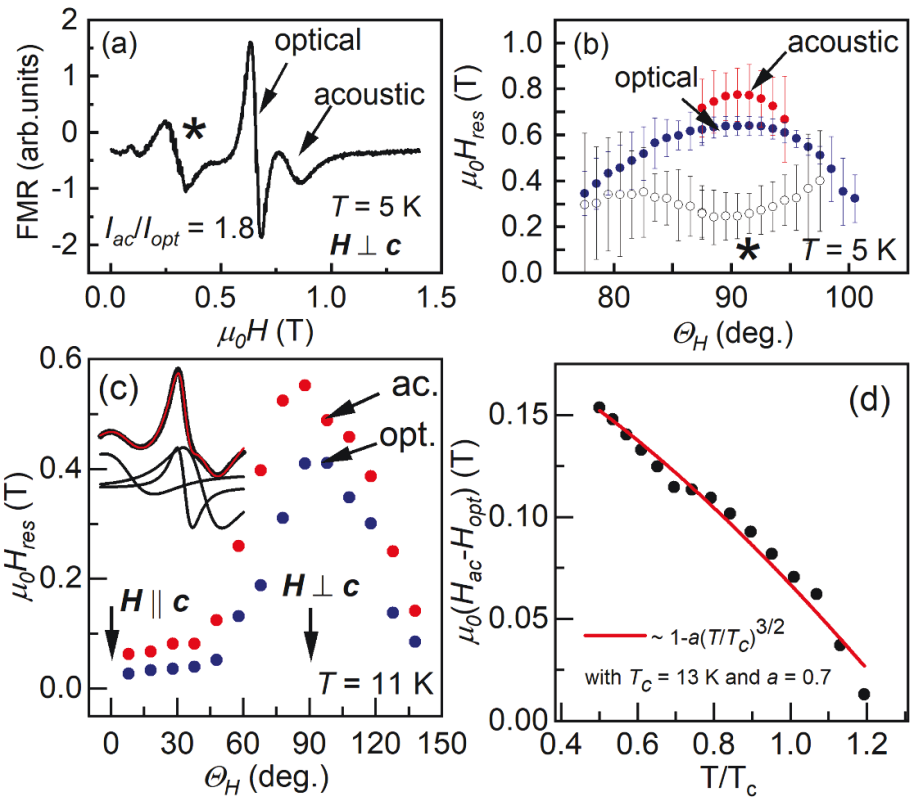

Figure 2. FMR in sample S2 showing separation of acoustic and optical resonance mode of coupled SLs and QLs. (a) FMR spectrum at 5 K around $\boldsymbol{H} \perp \boldsymbol{c}$ (90°). Optical and acoustic modes are indicated with arrows. Asterisk * marks the extra resonance line originating from the second solution of the Smit and Beljers equations (see also supplementary material and figure S2). (b) Anisotropy of resonance signals at 5 K. Error bars indicate line width. * marks the second solution of the Smit and Beljers equations. (c) Anisotropy of the resonance signal at 11 K. The inset shows a schematic decomposition of the measured signal into component lines, higher acoustic and lower optical modes. The third line at the lowest resonance field is due to the second solution of the Smit and Beljers equations. (d) Splitting between acoustic and optical modes at $\boldsymbol{H} \perp \boldsymbol{c}$ versus temperature.

At 5 K, the two component lines can be resolved only around $\boldsymbol{H}$ perpendicular to the Bi_2Te_3 $\boldsymbol{c}$ axis, θ_H between 77° and 100° in figure 2(b) (90° means the direction $\boldsymbol{H} \perp \boldsymbol{c}$). At 77° the lines merge and no resonance is detected until 0°, $\boldsymbol{H} \parallel \boldsymbol{c}$, due to the large magnetic anisotropy constant and insufficient applied microwave energy of the X-band. This effect can be tracked in figure S2(a) in the supplementary material (available online at stacks.iop.org/2DM/9/015026/mmedia), where the magnetization equilibrium angles are shown and discussed. At 11 K, however, one can recognize a typical anisotropy pattern (figure 2(c)) of two coupled spin subsystems with the easy axis anisotropy. Remarkably, the two modes never cross in the angular dependence, which is characteristic for FMR in coupled films and allows to distinguish them from the uncoupled layers. This can be understood as follows. For the two uncoupled layers with different anisotropies the resonance field for $\boldsymbol{H} \parallel \boldsymbol{c}$ of one layer will be higher than for the second layer, while for $\boldsymbol{H} \perp \boldsymbol{c}$ the situation will be the opposite. This would cause the two angular dependences to cross at a certain angle. For a coupled system, the two angular dependences are shifted relative to each other by an amount depending on the inter-layer coupling.

4. Phenomenological analysis of FMR in the multilayered $MnBi_2Te_4/(Bi_2Te_3)_n$

We adapt a well-established phenomenological model for FMR in two exchange coupled thin films [28] to a $MnBi_2Te_4$ and Mn doped Bi_2Te_3 multilayered material system, assuming that the spins in the respective subsystems see the same anisotropy and exchange fields, respectively [34]. For identical magnetic layers, the higher-lying acoustic mode is degenerate with that of a single layer while the optical mode (for $\boldsymbol{H} \parallel \boldsymbol{ab}$) is shifted from the single layer resonance towards a lower magnetic field by the exchange field H_{ex} equal to:

$$H_{ex} = \frac{2J}{M_s}\left(\frac{t_1 + t_2}{t_1 t_2}\right). \quad (1)$$

Here, J is the interlayer exchange energy per unit area, M_s is the saturation magnetization, t_1 and t_2 are thicknesses of the respective magnetic layers. At 5 K, the observed splitting between the acoustic and the optical mode is about 150 mT, which assuming in rough approximation equal magnetic anisotropy constants for $MnBi_2Te_4$ and for Mn doped Bi_2Te_3, gives the estimation of the exchange coupling constant

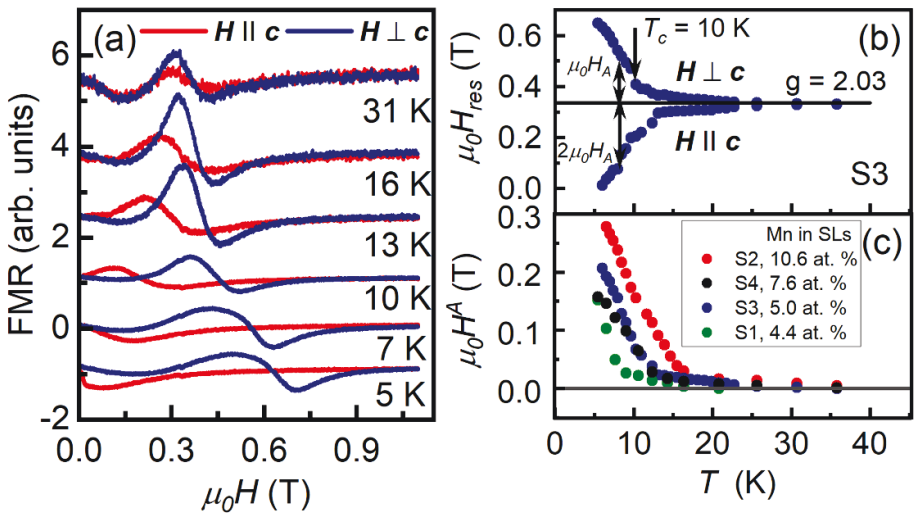

Figure 3. FMR of $MnBi_2Te_4/(Bi_2Te_3)_n$. (a) FMR spectra of sample S3 measured versus temperature for magnetic field applied parallel and perpendicular to the Bi_2Te_3 ***c*** axis. Single resonance line originates from similarity of magnetic anisotropy constants between $MnBi_2Te_4$ and Mn-doped Bi_2Te_3 and weak inter-layer coupling and allows to treat sample as a single-domain ferromagnetic material. (b) FMR anisotropy (resonance field for $\boldsymbol{H} \parallel \boldsymbol{c}$ and $\boldsymbol{H} \perp \boldsymbol{c}$, respectively) measured versus temperature for sample S3. (c) Anisotropy field determined from equation (6) versus temperature for S1–S4 samples. For sample S2 the average resonance field for acoustic and optical modes was used in equation (6). Complementary FMR measurement for samples S2 and S3 can be found in the supplementary material.

$J = 1.37 \times 10^{-7}$ J m^{-2}. Here, t_1 was assumed equal to the thickness of one SL, 1.68 nm, while t_2 to the thickness of four QLs, 5.12 nm, the saturation magnetization M_s is 150 emu mol^{-1} [3]. The temperature variation of the splitting between the acoustic and the optical mode is shown in figure 2(d). The $T^{3/2}$ power law can be applied, which according to [35] follows from thermal spin fluctuations at the interface that lead to the reduction of the effective interlayer coupling. Note that the apparent change in slope at about 0.7 shown in figure 2(d) is artificial, due to the wide and irregular shape of the resonance lines.

In the lower T_c samples (S2–S4) the FMR appears as a single, irregular resonance line (figure 3(a)) indicating weak coupling between $MnBi_2Te_4$ and Mn doped Bi_2Te_3 and comparable magnetic anisotropy constants. The FMR spectra can be conveniently approximated then by the uniform resonance mode with magnetic anisotropy constants treated as the magnetization-weighted mean values of the two spin subsystems [27]. The total free energy density U which takes into account the dominant effect of the axial anisotropy along the ***c*** axis can be expressed by:

$$U = -HM\left(\cos\theta\,\cos\theta_H + \sin\theta\,\sin\theta_H \cos\left(\varphi - \varphi_H\right)\right) - \frac{1}{2}M^2\sin^2\theta + K_1\sin^2\theta, \quad (2)$$

where the first term is the Zeeman term, the second term is the shape anisotropy energy and the third term is the axial anisotropy energy, approximated by the first element of a series expansion with anisotropy constant K_1. M and H are absolute values of the magnetization $\boldsymbol{M}$ and magnetic field $\boldsymbol{H}$ vectors, respectively. Angles θ, φ, θ_H, φ_H are polar and azimuthal angles for $\boldsymbol{M}$ and $\boldsymbol{H}$ in the spherical coordinate system, respectively. The polar ***z*** axis is along the Bi_2Te_3 ***c*** axis (the easy axis), the ***xy*** plane lies in the sample plane (***ab*** plane). Since demagnetization energy has the same dependence on θ as axial anisotropy energy, only the total effect is measured experimentally, which can be represented by the effective anisotropy field

$$H^{\mathrm{A}} = \frac{K_1}{M} - \frac{1}{2}M. \quad (3)$$

In the case of all studied $MnBi_2Te_4/(Bi_2Te_3)_n$, the easy axis is out-of-plane (along ***c*** direction) due to large and positive K_1. Because the magnetocrystalline anisotropy dominates over the demagnetization anisotropy, the FMR occurs at the lower magnetic field for $\boldsymbol{H}$ applied parallel to the ***c*** axis than for $\boldsymbol{H}$ applied perpendicular to it (figure 3(a)) like in $Bi_{2-x}Mn_xTe_3$ [32, 33]. This property generated great interest in this family of materials due to the magnetic impact on the TSSs caused by the out-of-plane component of magnetization.

The resonance field $H_{\mathrm{res}}(\theta_H)$ can be then obtained by standard Smit and Beljers formula [36],

$$\left(\frac{\omega}{\gamma}\right)^2 = \frac{1}{M^2\sin^2\theta}\left[\frac{\mathrm{d}^2U}{\mathrm{d}\theta^2}\frac{\mathrm{d}^2U}{\mathrm{d}\varphi^2} - \left(\frac{\mathrm{d}^2U}{\mathrm{d}\theta\mathrm{d}\varphi}\right)^2\right], \quad (4)$$

fulfilling simultaneously the conditions for minimum energy at equilibrium positions of magnetization, θ_{eq} and φ_{eq},

$$\left(\frac{\mathrm{d}U}{\mathrm{d}\theta}\right)_{\theta=\theta_{\mathrm{eq}},\varphi=\varphi_{\mathrm{eq}}} = \left(\frac{\mathrm{d}U}{\mathrm{d}\varphi}\right)_{\theta=\theta_{\mathrm{eq}},\varphi=\varphi_{\mathrm{eq}}} = 0. \quad (5)$$

Here ω is the angular frequency of the applied microwaves and γ is the gyromagnetic ratio. The resonance field varies with tilt angle θ_H around the average value $\omega\,\gamma^{-1}$, corresponding to $f = 9.5$ GHz of the applied microwave frequency and $g = 2.03$, extrapolated from the paramagnetic position of the resonance at higher temperatures (figure 3(b)) which is a typical value for highly localized Mn center [20]. The equilibrium position of magnetization will be discussed in the supplementary material. Remarkably, for large magnetic anisotropy constants with respect to the applied microwave frequency, two possible equilibrium angles exist. The second solution of the Smit and Beljers problem corresponds to the second resonance line appearing at the low magnetic field in the spectra, marked with * in figure 2.

The difference between resonance field for $\boldsymbol{H}$ applied parallel to the $\boldsymbol{c}$ axis and perpendicular to it is three times the anisotropy field:

$$H_{\mathrm{res}}(0^\circ) - H_{\mathrm{res}}(90^\circ) = 3H^{\mathrm{A}}. \quad (6)$$

The magnetic anisotropy field, H^{A}, determined from equation (6) is shown in figure 3(c). The highest anisotropy field is obtained for sample S2, $\mu_0 H^{\mathrm{A}} = 280$ mT at 6 K, which according to equation (3) corresponds to the anisotropy constant $K_1 = 407$ J m^{-3} for M being of the order of 150 emu mol^{-1} [3]. Typically, the anisotropy of the FMR signal is expected to scale with saturation magnetization [37]. However, while the magnetization tends to zero above the critical temperature in a way that only slightly deviates from the mean-field-like manner [3], the anisotropy of the FMR signal survives far above the T_c, up to about 40 K for all measured samples. This shows that the short-range magnetic correlations, with the net-zero overall impact on sample magnetization, are present above the critical temperature. The effect may originate from the two-dimensional (2D) character of the studied systemsince the 2D FM in applied magnetic field can form large-scale correlations in the paramagnetic regime above the T_c, which are sensitive to the orientation of the applied field relative to the anisotropy axis [38]. These effects are typically observed in the magnetic resonance of layered materials [32, 37, 39].

5. Surface electronic band structure under disorder, ARPES and DFT

After establishing the composition, structure, and magnetic properties of $MnBi_2Te_4/(Bi_2Te_3)_n$, we studied the influence of the disorder on the surface states using ARPES measurements and DFT calculations. ARPES data obtained at photon energies from 8 eV up to 54 eV are shown in figures 4(a)–(f). Surface bands of the $MnBi_2Te_4/(Bi_2Te_3)_n$ family have a complex orbital character which can be highlighted by appropriately selecting the sampling photon energy [40]. This is indeed visible in our data where intensities of the respective bands or their parts strongly vary with the applied photon energy. At 8 eV, the Dirac cone (TSS1) can be viewed analogous to TSSs of pristine Bi_2Te_3 [41–43], with the Dirac point located about 0.35 eV below the Fermi level (figure 4(a)). However, applied higher photon energies (between 24 eV and 54 eV) reveal a more complex structure in this region. In addition to the TSS1 states, a second Dirac cone (TSS2) and an extra parabolic band (CB1) appear (figures 4(e) and (f)). Such a parabolic band has previously been reported in the literature with an origin still under debate. Since DFT calculations of perfect structures do not reproduce the parabolic band, its origin was suggested to be a deviation from the ideal structure [10, 40, 44]. Finally, at intermediate photon energies (20 eV) a conduction band with linear dispersion (CB2) is observed. This measurement was done at about 6 K and all the bands remained essentially unchanged up to 120 K.

It has been previously discussed in the literature [10, 40] that surface states of $MnBi_2Te_4/(Bi_2Te_3)_n$ depend crucially on the surface termination type. One can distinguish a SL-terminated surface from a QL-SL-terminated surface. In the former, TSSs form a large magnetic gap of the order of 70–80 meV [3, 9, 11, 45], while in the latter, TSSs are hybridized with the valence band such that an anti-crossing gap is formed, which can be easily confused with the Dirac mass gap [10, 40]. Finally, for a QL-QL-SL-terminated surface, the surface bands resemble those for an unperturbed Bi_2Te_3 [10]. All these features are clearly visible in the DFT calculations in figures 4(g)–(i). In figure 4(g), a symmetric SL-4QL-SL structure was calculated to show the effect of the opening of the magnetic gap on the SL-terminated surface. The accepted thickness of the slab is sufficient to simulate topological electronic structure [46]. Red color denotes surface states localized on the topmost SL while blue color denotes the states localized on the bottommost SL. A Dirac mass gap of about 70 meV is shown. Our consideration of the SL-4QL-SL structure is justified since the band structure near the Fermi level is not affected by the number of QLs between the consecutive SLs, although the experimental sample (S3) has an average value $n = 7$ QLs. The same rationale is applied to the other surface termination types. Further, asymmetric slabs were investigated in order to assess disordered SL distribution in real crystals. QL-SL-2QL-SL and 2QL-SL-2QL-SL sequences were calculated as shown in figures 4(h) and (i), respectively. In these cases, the red and blue colors denote the states localized at the topmost QL and at the bottommost SL, respectively, while the orange color indicates states localized at the middle SL. This approach simultaneously simulates

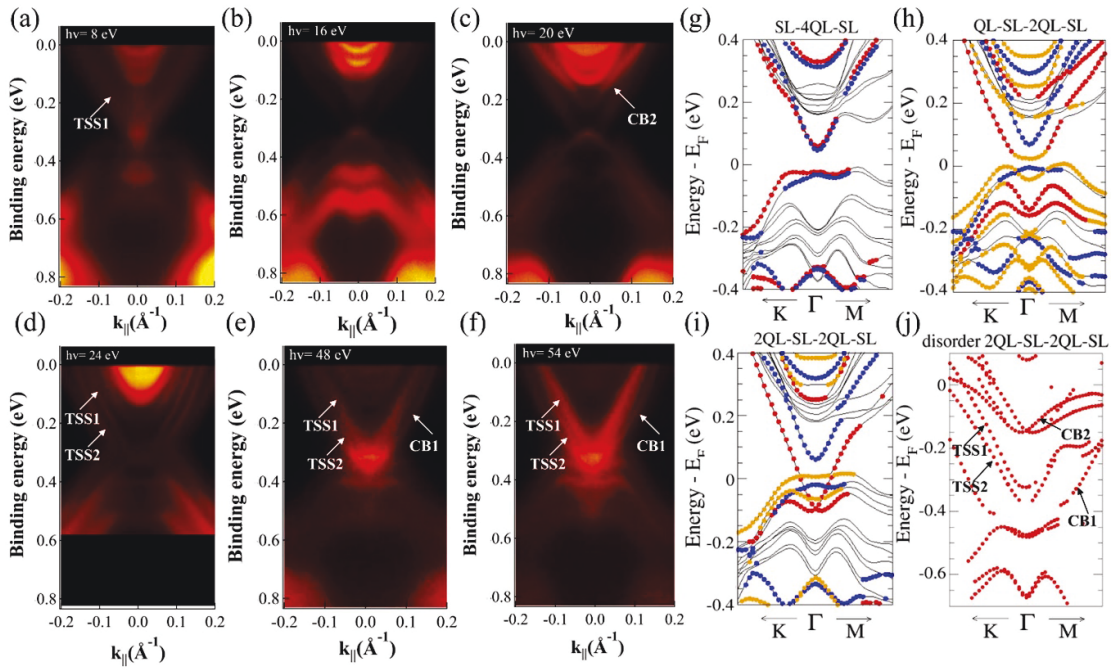

Figure 4. Surface electronic band structure of $MnBi_2Te_4/(Bi_2Te_3)_n$. (a)–(f) ARPES data of the disordered $MnBi_2Te_4/(Bi_2Te_3)_n$ (sample S3) obtained along $\Gamma \rightarrow M$ direction at photon energies 8 eV, 16 eV, 20 eV, 24 eV, 48 eV and 54 eV, respectively. (g)–(j) DFT-calculated band structures. The horizontal scale is the same as for ARPES. (g) SL (top)-4QL-SL (bottom), (h) QL (top)-SL-2QL-SL (bottom), (i) 2QL (top)-SL-2QL-SL (bottom), (j) 2QL-SL-2QL-SL with 50% of Mn atoms in SLs replaced by Bi. In (g) red color denotes surface states localized on the topmost SL while blue color denotes the states localized on the bottommost SL, (h), (i), the red (blue) color denotes the states where at least 40% of the electron density is localized at the topmost QL (bottommost SL), while the orange color means states where at least 40% of the electron density is localized at the middle SL. In (j), only the states where at least 28% of the electron density is localized at the topmost QL, are shown.

two different surface terminations. The anti-crossing of the Dirac cone (red) with valence band states (orange) characteristic for the QL-SL-terminated surface can be seen in figure 4(h). In figure 4(i), both the magnetic gap formed by blue bands of the SL-QL-terminated surface and almost unperturbed Bi_2Te_3 Dirac cone (red) of 2QL-SL-terminated surface is viewed.

Although it is possible that the large spot of the ARPES beam used in our experiments covers a non-uniform surface made of terraces with different terminations, so that the ARPES signal is a superposition of the corresponding images [47], we propose an alternative explanation of the recorded spectra, taking into account effects of the disorder. Notably, the electronic states of individual bands in perfect structures shown in figures 4(g)–(i) are all well localized on the respective QLs or SLs, 40% or more of the electron density is localized on the topmost layers. The situation changes dramatically when the disorder is introduced. In figure 4(j) 2QL-SL-2QL-SL structure was calculated with 50% of Mn atoms in SLs replaced by Bi. We compare it to the ARPES spectra of sample S3 for which EDX shows only 5.0 ± 0.8 at.% of Mn in SLs. The first striking difference compared to the analogous perfect structure shown in figure 4(i) is the delocalization of the wave functions. It is no longer possible to assign the respective bands to the corresponding QLs or SLs. Figure 4(j) shows thus the states localized at the topmost QL (28% or more of the electron density) in order to relate them to ARPES experiment probing finite depth of about 1 nm. The calculated band structure is qualitatively consistent with the ARPES data. One can identify the upper part of the parabolic band (CB1) while the bottom of the band has clearly a more bulk-like character. The double structure of the Dirac cone (TSS1 and TSS2) was also modeled successfully. Finally, the conduction band with linear dispersion (CB2) can be recognized as part of the Rashba-split band in figure 4(j). Only the linear part of the band is visible in the experiment. At the Γ point, its spectral weight decreases, possibly due to changes in its orbital character [40]. Furthermore, with the disorder in SLs, the DFT band structure shows TSS1, TSS2, CB1, CB2 below the Fermi level (zero in figure 4(j)), which is consistent with the ARPES data.

Performed DFT calculations (not shown) confirm, that both FM and AFM coupling between SLs lead to analogous band structures. On the contrary, neglecting magnetic coupling in a single SL causes the appearance of a gapless Dirac cone in the band gap on the SL-terminated surface. It means, that the disorder factor that can most strongly affect the structure of surface bands concerns the magnetic ordering within a single SL. Indeed, introducing magnetic disorder merely in a SL allowed to capture the most pronounced features in the ARPES data collected for the real world $MnBi_2Te_4/(Bi_2Te_3)_n$.

6. Discussion and conclusions

The disorder makes systemic changes to the properties of $MnBi_2Te_4/(Bi_2Te_3)_n$, affecting both the nature of the band structure through the delocalization of wave functions and introducing new bands, as well as influencing magnetic interactions—allowing the material to be treated as a stack of exchange coupled ultrathin layers. Quantitative description of the impact of the disorder on critical phase transition temperature is, however, challenging due to the number of factors that should be taken into account: the distance between SLs and its distribution, the missing fraction of Mn in SLs, and concentration of Mn in QLs as well as the thickness of the QL blocs (and its distribution). However, it is evident from the figure 3(c) that the magnitude of the magnetic anisotropy field, tracked by the T_c, correlates with the quality of a SL. The highest $T_c = 13$ K being obtained for sample S2 with the evaluated concentration of Mn in SLs equal to about 10.6 at.%, while the lowest $T_c = 6$ K for sample S1 with the highest deviation from the ideal structure, only 4.4 at.% of Mn in SLs. We note that the samples may additionally contain point defects, which are not evaluated in this work. Point defects can be significant in crystals that did not undergo the second step in Bridgman's growth process (e.g. sample S1, see section 7). Sample S3 with 5 at.% of Mn in a SL is an intermediate case. In turn, sample S4 ($n = 2$) deserves particular attention since it has the highest overall concentration of Mn, 4 at.% (7.6 at.% in a SL), but does not show T_c which is notably higher than its 2%-companion sample S3 (5 at.% of Mn in a SL). Here evidently, the shorter distance between SLs begins to play a role switching on AFM interactions between SLs with $n = 2$ and thus weakening FM exchange coupling. The obvious conclusion here arises, that in order to engineer material with high FM phase transition temperature, special attention should be paid to the quality of SLs while simultaneously performing doping of Mn into larger QL blocs. It is also worth noting that the $T^{3/2}$ power law applied to the splitting of the acoustic and optical modes, and thus to the interlayer exchange energy, suggests that the microscopic origin of the coupling in samples with higher n is dominated by interface effects. This would marginalize the role of the spacing between SLs in high n samples in defining T_c.

Summarizing, we analyzed the structure, composition and magnetic properties of the FM $MnBi_2Te_4/(Bi_2Te_3)_n$ with $n = 2, 4, 7 \pm 1$, and 12 ± 5. The complex system of the superlattice is strongly affected by disorder effects. In addition to the statistical distribution of the distance between SLs, which is the larger the higher is n, the omnipresent migration of Mn between SLs and QLs occurs: Mn is missing in SLs and substitutes into QLs. This has a pronounced impact on magnetic properties as deviation from the ideal structure must lower the strength of intra-layer magnetic ordering within a single SL because of the highly increased distance between planarly oriented Mn sites. Simultaneously the depleted SLs couple via an available population of Mn in QLs and the system is ferromagnetically stabilized in the three-dimensions. Disordered $MnBi_2Te_4/(Bi_2Te_3)_n$ typically appears as a single-domain FM, showing up in FMR as a uniform resonance mode, due to small inter-layer exchange coupling parameter (maximum value found $J = 1.37 \times 10^{-7}$ J m^{-2}) and similarity of magnetic anisotropy constants between $MnBi_2Te_4$ and Mn-doped Bi_2Te_3. Mn migration between QLs and SLs evidently makes $MnBi_2Te_4/(Bi_2Te_3)_n$ avoid magnetic differentiation in the component layers. We note that for samples with higher T_c the optical and acoustic modes of two spin subsystems can be experimentally resolved.

The disorder changes the surface electronic structure, in particular causing the appearance of a parabolic band CB1 and another trivial conduction band CB2 with linear dispersion, which can be easily confused with a gapped Dirac cone on a SL-terminated surface. Moreover, the Dirac cone of the QL-terminated surface evolves into peculiar double structure, which without a doubt requires further studies, in particular of its spin texture. Remarkably, all electron states that are well localized on respective QLs or SLs in perfect structures, in disordered material become delocalized. Finally, we remark that being aware and understanding the impact of the disorder on the surface states in intrinsic topological magnets is crucial to identify fingerprints for the large Dirac mass gap on the SL-terminated surfaces in ARPES experiments. The presence of such a gap is still under debate despite numerous studies performed.

7. Methods

Samples for the studies were grown by vertical and horizontal variants of the Bridgman method in Kurnakov Institute of General and Inorganic Chemistry, Russian Academy of Sciences (vertical furnace) and in the Institute of Physics, Polish Academy of Sciences (horizontal furnace). The elements used in both growth processes were high purity (99.999%) bismuth (Bi), tellurium (Te) and manganese (Mn). In the vertical method, the material was first synthesized in quartz ampules evacuated to 10^{-4} Pa. The ampules were loaded into a furnace, heated to 900 K, and maintained at this temperature for 48 h to achieve better homogenization. Then they were cooled down at a rate of 60 K h^{-1} to 550 K and annealed for 24 h. Then the furnace was switched off and cooled down to room temperature. In the next step, the synthesized material was ground and loaded into the evacuated ampules (about 10^{-4} Pa) and sealed. To obtain a homogenized solution, the growing material was heated to 1073 K and rotated along the ampule axis for five days in the hot part of the furnace. Then the

ampules were moved down at a speed of 2 mm d^{-1}. The temperature in the lower part of the furnace was kept at 873 K. This procedure resulted in crystals with average sizes of 50 mm in length and 14 mm in diameter. In the horizontal method, the quartz ampules sealed under vacuum (about 10^{-4} Pa) were placed in the furnace containing two heating zones. In the first step, the ampules were heated up to a temperature of about 1053 K for 48 h to synthesize the compound and to homogenize the melt. Then the ampules were cooled down to the temperature of 903 K. Next, the ampules were pulled through the temperature gradient equal to 10 K cm^{-1} at a rate of 1 mm h^{-1}. The single crystals obtained this way had average dimensions of 50 mm × 10 mm × 8 mm.

Structural studies were performed using two magnification scales offered by SEM and TEM. SEM investigations were performed using a Hitachi SU-70 microscope equipped with a Thermo Scientific EDX spectrometer with silicon drift detector and Noran System 7 allowing for morphology and chemical composition studies. TEM investigations were carried out by the FEI Talos F200X microscope operated at 200 kV. High-resolution structural observations were performed in STEM mode using HAADF imaging. EDX spectroscopy using a Super-X system with four SDDs (silicon drift detectors) was applied to the detection of differences in local chemical composition. The samples for TEM investigations were cut along the *c* axis, in the [11$\underline{2}$0] orientation, using a focused ion beam method. Additionally, SIMS was carried out using a time-of-flight analyzer (IONTOF GmbH) enabling depth profiling.

FMR measurements were performed using Bruker ELEXSYS-E580 electron paramagnetic resonance spectrometer operating in X-band (9.5 GHz), at temperatures varied by continuous-flow Oxford helium cryostat. Due to the use of magnetic field modulation and the lock-in technique the resonance signal represents the field derivative of the absorbed microwave power.

ARPES measurements were carried out at the National Synchrotron Radiation Centre SOLARIS in Cracow, Poland at the variable polarization UARPES beamline. Samples were glued with epoxy resin to a sample holder and cleaved in an ultra-high vacuum via mechanical exfoliation. As a photon source elliptically polarizing undulator APPLE II type was used. Experimental data were collected by VGScienta DA30L electron spectrometer with an energy and angle resolution of 3 meV and 0.1°, respectively.

DFT calculations were performed using VASP code [48, 49]. We used projector-augmented-wave pseudopotentials [50, 51] and Perdew–Burke–Ernzerhof [52] generalized gradient approximation for the exchange-correlation functional. Spin–orbit coupling was included with an on-site Coulomb repulsion term $U = 5.34$ eV, chosen in order to take into account the strong correlation of Mn d orbitals, as discussed in supplementary note 3 of [9]. We also checked independently that the band structures we studied do not change much with a small change of the U value (not shown). The structures of SL-4QL-SL and 2QL-SL-2QL-SL with and without Mn disorder were fully relaxed until the residual forces are less than 0.01 eV $Å^{-1}$, while the structure of QL-SL-2QL-SL was constructed from the experimental structures of $MnBi_2Te_4$ [53] and Bi_2Te_3 [54]. We confirm that the effect of geometry relaxation is negligible. For the three structures without the disorder, 11 × 11 × 1 k-points were sampled, while for the structure with 50% Mn disorder, 5 × 5 × 1 k-points were sampled since a supercell of 2 × 2 surface atoms was used to incorporate the disorder effect. In the supercell, 50% of the Mn atoms in each SL is replaced by Bi.

Data availability statement

All data that support the findings of this study are included within the article (and any supplementary files).

Acknowledgments

This work was supported by the Polish National Science Center (NCN) Grant 2016/21/B/ST3/02565. Computational support for Kyungwha Park was provided by Virginia Tech ARC and San Diego Supercomputer Center (SDSC) under DMR-060009N. Work at the CCNY was supported by NSF Grants DMR-2011738 and HRD-1547830.

ORCID iDs

Irina Abaloszewa https://orcid.org/0000-0003-4372-6410
Bogdan J Kowalski https://orcid.org/0000-0003-4821-5265
Marcin Konczykowski https://orcid.org/0000-0003-3376-5635
Agnieszka Wołoś https://orcid.org/0000-0002-0650-2285

References

[1] Mogi M, Kawamura M, Yoshimi R, Tsukazaki A, Kozuka Y, Shirakawa N, Takahashi K S, Kawasaki M and Tokura Y 2017 A magnetic heterostructure of topological insulators as a candidate for an axion insulator *Nat. Mater.* **16** 516–21
[2] Liu C-X, Zhang S-C and Qi X-L 2016 The quantum anomalous Hall effect: theory and experiment *Annu. Rev. Condens. Matter Phys.* **7** 301–21
[3] Deng H *et al* 2021 High-temperature quantum anomalous Hall regime in a $MnBi_2Te_4/Bi_2Te_3$ superlattice *Nat. Phys.* **17** 36–42
[4] Grauer S, Fijalkowski K M, Schreyeck S, Winnerlein M, Brunner K, Thomale R, Gould C and Molenkamp L W 2017

Scaling of the quantum anomalous Hall effect as an indicator of axion electrodynamics *Phys. Rev. Lett.* **118** 246801
[5] Xiao D *et al* 2018 Realization of the axion insulator state in quantum anomalous Hall sandwich heterostructures *Phys. Rev. Lett.* **120** 56801
[6] Deng Y, Yu Y, Shi M Z, Guo Z, Xu Z, Wang J, Chen X H and Zhang Y 2020 Quantum anomalous Hall effect in intrinsic magnetic topological insulator $MnBi_2Te_4$ *Science* **367** 895–900
[7] Gu M, Li J, Sun H, Zhao Y, Liu C, Liu J, Lu H and Liu Q 2021 Spectral signatures of the surface anomalous Hall effect in magnetic axion insulators *Nat. Commun.* **12** 3524
[8] Lei C, Chen S and MacDonald A H 2020 Magnetized topological insulator multilayers *Proc. Natl Acad. Sci. USA* **117** 27224–30
[9] Otrokov M M *et al* 2017 Highly-ordered wide bandgap materials for quantized anomalous Hall and magnetoelectric effects *2D Mater.* **4** 025082
[10] Klimovskikh I I *et al* 2020 Tunable 3D/2D magnetism in the $(MnBi_2\ Te_4)(Bi_2Te_3)_m$ topological insulators family *npj Quantum Mater.* **5** 54
[11] Otrokov M M *et al* 2019 Prediction and observation of an antiferromagnetic topological insulator *Nature* **576** 416–22
[12] Otrokov M M, Rusinov I P, Blanco-Rey M, Hoffmann M, Vyazovskaya A Y, Eremeev S V, Ernst A, Echenique P M, Arnau A and Chulkov E V 2019 Unique thickness-dependent properties of the van der Waals interlayer antiferromagnet $MnBi_2Te_4$ films *Phys. Rev. Lett.* **122** 107202
[13] Rienks E D L *et al* 2019 Large magnetic gap at the Dirac point in $Bi_2Te_3/MnBi_2Te_4$ heterostructures *Nature* **576** 423–8
[14] Wang P, Ge J, Li J, Liu Y, Xu Y and Wang J 2021 Intrinsic magnetic topological insulators *Innovation* **2** 100098
[15] Wimmer S *et al* 2021 Mn-rich $MnSb_2Te_4$: a topological insulator with magnetic gap closing at high Curie temperatures of 45–50 K *Adv. Mater.* **33** 212935
[16] de Jong N, Frantzeskakis E, Zwartsenberg B, Huang Y K, Wu D, Hlawenka P, Sańchez-Barriga J, Varykhalov A, van Heumen E and Golden M S 2015 Angle-resolved and core-level photoemission study of interfacing the topological insulator $Bi_{1.5}Sb_{0.5}Te_{1.7}Se_{1.3}$ with Ag, Nb, and Fe *Phys. Rev.* B **92** 075127
[17] Li J, Li Y, Du S, Wang Z, Gu B-L, Zhang S-C, He K, Duan W and Xu Y 2019 Intrinsic magnetic topological insulators in van der Waals layered $MnBi_2Te_4$-family materials *Sci. Adv.* **5** eabg5685
[18] Eremeev S V, Otrokov M M and Chulkov E V 2018 New universal type of interface in the magnetic insulator/topological insulator heterostructures *Nano Lett.* **18** 6521–9
[19] Yan C, Zhu Y, Fernandez-Mulligan S, Green E, Mei R, Yan B, Liu C, Mao Z and Yang S 2021 Delicate ferromagnetism in $MnBi_6Te_{10}$ (arXiv:2107.08137 [cond-mat.mtrl-sci])
[20] Wolos A *et al* 2016 High-spin configuration of Mn in Bi_2Se_3 three-dimensional topological insulator *J. Magn. Magn. Mater.* **419** 301–8
[21] Růžička J *et al* 2015 Structural and electronic properties of manganese-doped Bi_2Te_3 epitaxial layers *New J. Phys.* **17** 9–20
[22] Lee I *et al* 2015 Imaging Dirac-mass disorder from magnetic dopant atoms in the ferromagnetic topological insulator $Cr_x(Bi_{0.1}Sb_{0.9})_{2-x}Te_3$ *Proc. Natl Acad. Sci. USA* **112** 1316–21
[23] Liu Y *et al* 2021 Site mixing for engineering magnetic topological insulators *Phys. Rev.* X **11** 021033
[24] Liu C *et al* 2020 Distinct quantum anomalous Hall ground states induced by magnetic disorders *Phys. Rev.* X **10** 18–27
[25] Heinrich B 2005 Ferromagnetic Resonance in Ultrathin Film Structures *Ultrathin Magnetic Structures II* ed B Heinrich and J A C Bland (Berlin: Springer) 195–222
[26] Linder J and Baberschke K 2003 Ferromagnetic resonance in ultra-thin films *J. Phys.: Condens. Matter* **15** S469–78
[27] Heinrich B and Cochran J F 1998 Ultrathin metallic magnetic films: magnetic anisotropies and exchange interactions *Adv. Phys.* **42** 523–639
[28] Zhang Z, Zhou L, Wigen P E and Ounadjela K 1994 Angular dependence of ferromagnetic resonance in exchange-coupled Co/Ru/Co trilayer structures *Phys. Rev.* B **50** 6094–112
[29] Souchay D *et al* 2019 Layered manganese bismuth tellurides with $GeBi_4Te_7$- and $GeBi_6Te_{10}$-type structures: towards multifunctional materials *J. Mater. Chem.* C **7** 9939–53
[30] Wu J, Liu F, Liu C, Wang Y, Li C, Lu Y, Matsuishi S and Hosono H 2020 Toward 2D magnets in the $(MnBi_2Te_4)(Bi_2Te_3)_n$ bulk crystal *Adv. Mater.* **32** 2001815
[31] Shao J *et al* 2021 Pressure-tuned intralayer exchange in superlattice-like $MnBi_2Te_4/(Bi_2Te_3)_n$ topological insulators *Nano Lett.* **21** 5874–80
[32] Zimmermann S, Steckel F, Hess C, Ji H W, Hor Y S, Cava R J, Büchner B and Kataev V 2016 Spin dynamics and magnetic interactions of Mn dopants in the topological insulator Bi_2Te_3 *Phys. Rev.* B **94** 125205
[33] Hor Y S *et al* 2010 Development of ferromagnetism in the doped topological insulator $Bi_{2-x}Mn_xTe_3$ *Phys. Rev.* B **81** 195203
[34] Keffer F and Kittel C 1952 Theory of antiferromagnetic resonance *Phys. Rev.* **85** 329–37
[35] Almeida N S, Mills D L and Teitelman M 1995 Temperature variation of the interfilm exchange in magnetic multilayers: the influence of spin wave interactions *Phys. Rev. Lett.* **75** 733–6
[36] Smit J and Beljers H G 1955 Ferromagnetic resonance absorption in BaFeO, a highly anisotropic crystal *Philips Res. Rep.* **10** 113–30
[37] Zeisner J, Alfonsov A, Selter S, Aswartham S, Ghimire M P, Richter M, van den Brink J, Buchner B and Kataev V 2019 Magnetic anisotropy and spin-polarized two-dimensional electron gas in the van der Waals ferromagnet $Cr_2Ge_2Te_6$ *Phys. Rev.* B **99** 165109
[38] Pini M G, Politi P and Stamps R L 2005 Anisotropy effects on the magnetic excitations of a ferromagnetic monolayer below and above the Curie temperature *Phys. Rev.* B **72** 014454
[39] Zeisner J, Mehlawat K, Alfonsov A, Roslova M, Doert T, Isaeva A, Büchner B and Kataev V 2020 Electron spin resonance and ferromagnetic resonance spectroscopy in the high-field phase of the van der Waals magnet $CrCl_3$ *Phys. Rev. Mater.* **4** 64406
[40] Vidal R C *et al* 2021 Orbital complexity in intrinsic magnetic topological insulators $MnBi_4Te_7$ and $MnBi_6Te_{10}$ *Phys. Rev. Lett.* **126** 176403
[41] Chen Y L *et al* 2009 Experimental realization of a three-dimensional topological insulator, Bi_2Te_3 *Science* **325** 178–81
[42] Chen C *et al* 2012 Robustness of topological order and formation of quantum well states in topological insulators exposed to ambient environment *Proc. Natl Acad. Sci. USA* **109** 3694–8
[43] Li Y-Y *et al* 2010 Intrinsic topological insulator Bi_2Te_3 thin films on si and their thickness limit *Adv. Mater.* **22** 4002–7
[44] Vidal R C *et al* 2019 Surface states and Rashba-type spin polarization in antiferromagnetic $MnBi_2Te_4$ (0001) *Phys. Rev.* B **100** 121104(R)
[45] Wu J *et al* 2019 Natural van der Waals heterostructural single crystals with both magnetic and topological properties *Sci. Adv.* **5** eaax9989
[46] Park K, Heremans J J, Scarola V W and Minic D 2010 Robustness of topologically protected surface states in layering of Bi_2Te_3 thin films *Phys. Rev. Lett.* **105** 186801
[47] Zhong H, Bao C, Wang H, Li J, Yin Z, Xu Y, Duan W, Xia T-L and Zhou S 2021 Light-tunable surface state and hybridization gap in magnetic topological insulator $MnBi_8Te_{13}$ *Nano Lett.* **21** 6080–6
[48] Kresse G and Furthmüller J 1996 Efficiency of *ab-initio* total energy calculations for metals and semiconductors

using a plane-wave basis set *Comput. Mater. Sci.* **6** 15–50
[49] Kresse G and Furthmuller J 1996 Efficient iterative schemes for *ab initio* total-energy calculations using a plane-wave basis set *Phys. Rev.* B **54** 11169–86
[50] Blöchl P E 1994 Projector augmented-wave method *Phys. Rev.* B **50** 17953–79
[51] Kresse G and Joubert D 1999 From ultrasoft pseudopotentials to the projector augmented-wave method *Phys. Rev.* B **59** 1758–75
[52] Perdew J P, Burke K and Ernzerhof M 1996 Generalized gradient approximation made simple *Phys. Rev. Lett.* **77** 3865–8
[53] Lee D S, Kim T-H, Park C-H, Chung C-Y, Lim Y S, Seo W-S and Park H-H 2013 Crystal structure, properties and nanostructuring of a new layered chalcogenide semiconductor, Bi_2MnTe_4 *CrystEngComm* **15** 5532–8
[54] Nakajima S 1963 The crystal structure of $Bi_2Te_{3-x}Se_x$ *J. Phys. Chem. Solids* **24** 479–85